How to cite: *Angew. Chem. Int. Ed.* **2021**, *60*, 16200–16207
International Edition: doi.org/10.1002/anie.202105307
German Edition: doi.org/10.1002/ange.202105307

Methane-to-Methanol

Methane-to-Methanol on Mononuclear Copper(II) Sites Supported on Al_2O_3: Structure of Active Sites from Electron Paramagnetic Resonance**

Jordan Meyet, Anton Ashuiev, Gina Noh, Mark A. Newton, Daniel Klose, Keith Searles, Alexander P. van Bavel, Andrew D. Horton, Gunnar Jeschke, Jeroen A. van Bokhoven, and Christophe Copéret**

Abstract: *The selective conversion of methane to methanol remains one of the holy grails of chemistry, where Cu-exchanged zeolites have been shown promote this reaction under stepwise conditions. Over the years, several active sites have been proposed, ranging from mono-, di- to trimeric Cu^{II}. Herein, we report the formation of well-dispersed monomeric Cu^{II} species supported on alumina using surface organometallic chemistry and their reactivity towards the selective and stepwise conversion of methane to methanol. Extensive studies using various transition alumina supports combined with spectroscopic characterization, in particular electron paramagnetic resonance (EPR), show that the active sites are associated with specific facets, which are typically found in γ- and η-alumina phase, and that their EPR signature can be attributed to species having a tri-coordinated $[(Al_2O)CuIIO(OH)]^-$ T-shape geometry. Overall, the selective conversion of methane to methanol, a two-electron process, involves two monomeric Cu^{II} sites that play in concert.*

Introduction

The direct and selective conversion of CH_4 to CH_3OH could transform the petrochemical industry, by enabling on-site conversion of CH_4 on a scale much smaller than is currently viable. Existing routes, which are both energy-intensive and indirect, require the generation of syngas (H_2/CO) through CH_4 reforming, which can then be converted to CH_3OH. Cheap and abundant CH_4 is the main constituent of natural gas (70–90%), but its transportation in liquid form is energy demanding and comes at additional cost. Although the development of catalytic processes for the partial oxidation of CH_4 is highly desirable, this reaction remains challenging due to the low reactivity of CH_4 compared to that of CH_3OH which leads to facile generation of over-oxidized and unwanted products (e.g. CO, CO_2).[1–4] In nature, methane monooxygenases (MMOs, with either Fe or Cu active sites) are highly efficient at performing this selective oxidation.[5] The particulate form of this enzyme (pMMO) possesses several copper-containing sites for which the exact structure and nuclearity are still under debate.[6–8] Initial studies ascribed the active site as a dimeric copper species present in the PmmoB subunit (Cu_B, Figure 1a).[9] A more recent report, supported by electron paramagnetic resonance (EPR) spectroscopy, however, has shown the exclusive presence of mononuclear sites in pMMO; the Cu_C site located in the PmmoC subunit has been assigned to the metal binding site responsible for hydrocarbon binding and oxidation (Figure 1a).[8]

In parallel, promising processes based on inorganic materials have been developed in recent years. These processes rely on chemical looping, which decouples an aerobic (O_2) oxidation step from the CH_4 activation step, and therefore curtails over-oxidation of the methoxy species formed.[10,11] The most-studied materials within the chemical looping paradigm are copper-exchanged zeolites. Different types of active centers have been proposed based on spectroscopic characterization.[12] These proposals include a dinuclear mono-μ-oxo $[Cu\text{-}O\text{-}Cu]^{2+}$ center[13] (Figure 1a) and a trinuclear $[Cu_3O_3]^{2+}$ core.[14] In addition, monomeric Cu sites $[CuOH]^+$ in chabazite,[15] and two monomers present in mordenite have been proposed based on density functional theory (DFT) calculations.[16] Recently, the formation of

[*] J. Meyet, A. Ashuiev, Dr. G. Noh, Dr. M. A. Newton, Dr. D. Klose, Dr. K. Searles, Prof. Dr. G. Jeschke, Prof. Dr. J. A. van Bokhoven, Prof. Dr. C. Copéret
Department of Chemistry and Applied Biosciences, ETH Zurich
Vladimir-Prelog-Weg 1–5, 8093 Zürich (Switzerland)
E-mail: ccoperet@ethz.ch
Prof. Dr. J. A. van Bokhoven
Laboratory for Catalysis and Sustainable Chemistry, Paul Scherrer Institute
5232 Villigen (Switzerland)
E-mail: jeroen.vanbokhoven@chem.ethz.ch
Dr. A. P. van Bavel, Dr. A. D. Horton
Shell Global Solutions International B.V.
Grasweg 31, 1031 HW Amsterdam (The Netherlands)

[**] A previous version of this manuscript has been deposited on a preprint server (https://doi.org/10.26434/chemrxiv.13295879.v2).
Supporting information and the ORCID identification number(s) for the author(s) of this article can be found under: https://doi.org/10.1002/anie.202105307.

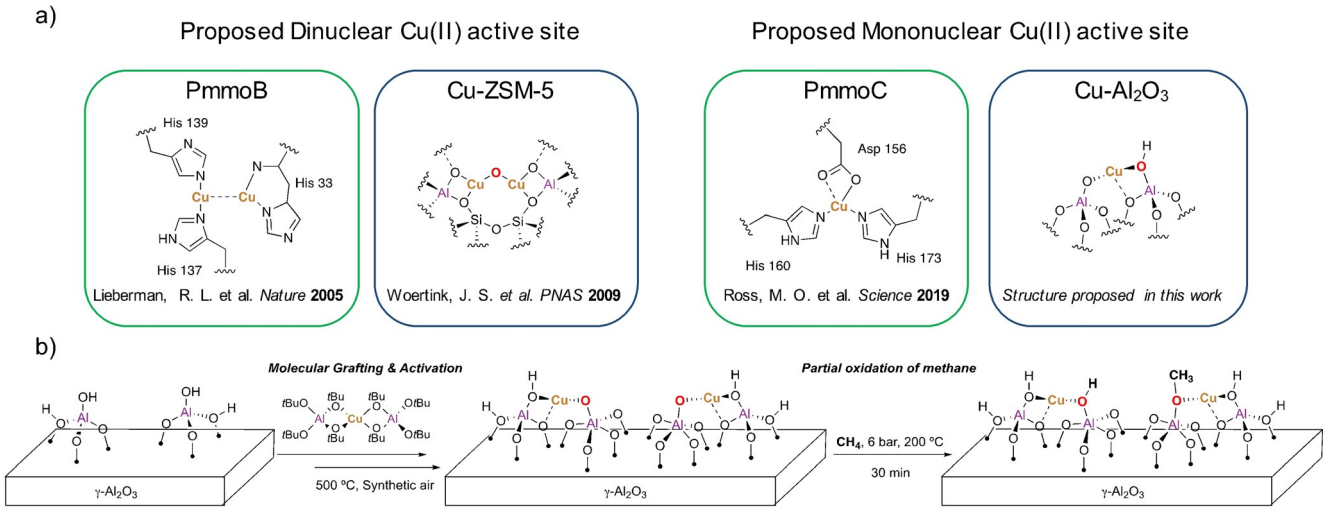

Figure 1. a) Proposed dinuclear (left) and mononuclear (right) active sites in the enzyme Pmmo (green frame) and the equivalent (in terms of copper nuclearity) analogues proposed for Cu supported on oxide supports (blue frame); b) The strategy used to generate monomeric Cu^{II} sites in a pure alumina environment and the subsequent reaction with CH_4 to form hydroxy and methoxy species.

paired monomeric $[CuOH]^+$ in zeolite Omega has been reported using anomalous X-ray diffraction.[17] However, despite major efforts, the active site structures remain highly debated. This deficit notwithstanding, substantial improvements in CH_3OH yield per chemical looping cycle have been achieved to reach the theoretical limit of CH_3OH for two Cu^{II} sites.[18] However, state-of-the-art zeolite-based materials remain economically unviable for commercial applications because of an insufficient amount of reactive sites per unit mass and the long cycle times associated with this step-wise process.[19,20] Thus, alternate materials must be explored for this challenging transformation. While the discovery of more efficient materials is of great importance to overcome some limitations faced by zeolites materials, the identification and characterization of the reactive centers is required to provide a structure/reactivity relationship as a guideline to improve material performance. Among possible alternative materials explored, copper supported on silica is shown to produces CH_3OH,[21–23] however the obtained yield is low and the active sites are ill-defined (small CuO clusters).

Recently, we showed that proximal monomeric Cu^{II} sites on alumina in an aluminosilicate environment, that resembled this of zeolites, could convert CH_4 to CH_3OH.[24] The material was generated via the surface organometallic chemistry (SOMC) and thermolytic molecular precursor (TMP) approach,[25] allowing the formation of highly-dispersed Cu^{II} centers with a coordination sphere dictated by the choice of tailored molecular precursor. However, the mixed (Si/Al) surface environment arising from the use of Cu^{II} siloxide precursors, necessary to reproduce the chemical environment found in zeolites, also led to the formation of multiple sites and prevented to obtain any detailed structural characterization of the reactive Cu^{II} sites.

We thus reasoned that the formation of well-dispersed Cu^{II} in a pure alumina environment, using a copper-aluminate molecular precursor, would enable the identification of the active site structure while keeping the high reactivity of these Cu^{II} sites (Figure 1b) even if the reactivity of Cu^{II} centers in a pure aluminum environment is yet to be explored.

Herein we describe the formation of well-dispersed Cu^{II} sites on γ-alumina using the SOMC/TMP approach, and extend the scope of the study to different transition alumina (θ, δ, α) to understand the influence of the support on the formation of reactive centers. Further analysis of the best performing material by EPR spectroscopy and reactivity with CO as probe molecule was then used to identify the structure of the active sites. In particular, in situ EPR spectroscopy allows for the spectroscopic identification of reactive Cu^{II} surface sites involved in the selective partial oxidation of CH_4. These reactive sites display a unique EPR signature, which can be observed for Cu^{II} on γ-, η- and θ-Al_2O_3 but not for non-defective α-Al_2O_3. Combining X-ray absorption spectroscopy (XAS), advanced EPR methods and computational modeling enabled the assignment of the reactive monomeric Cu^{II} sites on alumina as a tri-coordinated $[(Al_2O)CuO(OH)]^-$ species.

Results and Discussion

The copper aluminate molecular precursor,[26] $[Cu(\kappa^2\text{-}Al(OtBu)_4)_2]$ (**1**) (see Supporting Information, Section 3, Figures S1–S5 for the full characterization of **1**) was grafted on γ-Al_2O_3 ("γ-a") dehydroxylated under vacuum at varied temperatures (denoted by X in degree Celsius in "γ-a_X"): **γ-a_{500}** (OH density, $\Theta = 2.4$ OH nm^{-2}), **γ-a_{700}** ($\Theta = 0.9$ OH nm^{-2}) and **γ-a_{800}** ($\Theta = 0.4$ OH nm^{-2}) (see also Supporting Information, Figures S6 and S7), to yield the corresponding grafted materials **1-γ-a_X**. These grafted materials were characterized by UV–Vis, diffuse reflectance infrared (DRIFTS), EPR and X-ray absorption near-edge spectroscopies (XANES) (Supporting Information, Section 4, Figures S7–S9). All **1-γ-a_{X00}** materials show similar spectroscopic features, indicating the generation of similar surface species after grafting irrespective of the initial dehydroxylation temperature for γ-Al_2O_3. The presence of Cu^{II} was confirmed by both EPR and the

observation in the electronic spectra of the d-d transition characteristic of Cu^{II} species. However, the presence of a pre-edge feature at 8983 eV in the XANES, characteristic of Cu^{I} species, indicates the partial reduction of Cu (Figure S9), as previously observed when different Cu^{II} precursors were grafted on alumina.[24]

Thermal activation of these **1-γ-a$_X$** materials under a flow of dry synthetic air at 500 °C leads to the exclusive generation of organic-free Cu^{II} surface species (**1$_{500}$-γ-a$_X$**), as demonstrated by IR, UV–Vis, EPR and XANES (Section 4, Figures S10–S12). Possible auto-reduction of the Cu center under thermal activation, as previously reported for zeolitic materials,[27,28] can be excluded as no pre-edge features for Cu^{I} could be observed in the XANES spectra (Figure S12). Continuous wave (CW) X-band EPR analysis of the activated material (Figure S12) shows the presence of paramagnetic Cu^{II} species in a nearly axial environment ($g_{\parallel} > g_{\perp} > g_e$) with well-resolved Cu hyperfine coupling, which confirms the presence of monomeric Cu^{II} species well-dispersed on the alumina support.[24] Comparison of the CW EPR spectra amongst the activated Cu generated on the partially dehydroxylated alumina at different temperatures (vide infra), allows the identification of at least two different Cu species based on the observed parallel transitions ($A_{\parallel}$ and $g_{\parallel}$): $A_{\parallel} \approx 370$ MHz and $g_{\parallel} \approx 2.39$ for one site (denoted site I) and $A_{\parallel} \approx 440$ MHz and $g_{\parallel} \approx 2.33$ for the remainder of the signal (denoted site II, but which is composed of multiple species; vide infra) (Figure S12).

The ratio between these two sites is highly dependent on the initial dehydroxylation temperature of the alumina support prior to grafting. A dehydroxylation temperature of 500 °C (**1$_{500}$-γ-a$_{500}$**) yields predominantly site I, whereas dehydroxylation at 800 °C (**1$_{500}$-γ-a$_{800}$**) gives primarily site II.

The activated materials, **1$_{500}$-γ-a$_X$**, were reacted under 6 bars of CH_4 at 200 °C for 30 min and isolated under inert conditions for further spectroscopic characterization. DRIFTS analysis after reaction shows the appearance of two bands at 2957 and 2853 cm^{-1} assigned to the asymmetric and symmetric stretch of methoxy surface species, respectively (Figure S13).[29]

This assignment was confirmed by ^{13}C solid-state nuclear magnetic resonance (SSNMR) of **1$_{500}$-γ-a$_{500}$** reacted with $^{13}CH_4$, where two distinct peaks are observed in the ^{13}C NMR spectra: a major broad peak at 48.3 ppm along with a minor peak at 64 ppm, assigned, respectively to surface methoxy/methanol ($CH_3O(H)$-) and small amounts of dimethyl ether (DME) (Figure S14).[30] DME is the only side product observed in **1$_{500}$-γ-a$_{500}$** under reaction conditions according to NMR and infrared spectroscopy.

After extraction with water at 120 °C, the **1$_{500}$-γ-a$_{500}$** material shows the highest CH_3OH productivity among all samples with 0.12 mol $CH_3OH\,mol^{-1}$ of Cu. The CH_3OH yields for the other materials are lower, with **1$_{500}$-γ-a$_{800}$** yielding only half the amount of CH_3OH (0.06 mol $CH_3OH\,mol^{-1}$ of Cu; Supporting Information, Table 1). A recycling study was also performed using **1-γ-a$_{700}$** calcined at 700 °C (**1$_{700}$-γ-a$_{700}$**) showing similar CH_3OH yields before and after recycling with ca. 0.09 $CH_3OH\,mol^{-1}$ of Cu (Supporting Information, Table S1). The reaction of γ-Al_2O_3 in the absence of Cu sites under similar conditions does not yield any CH_3OH products.[24]

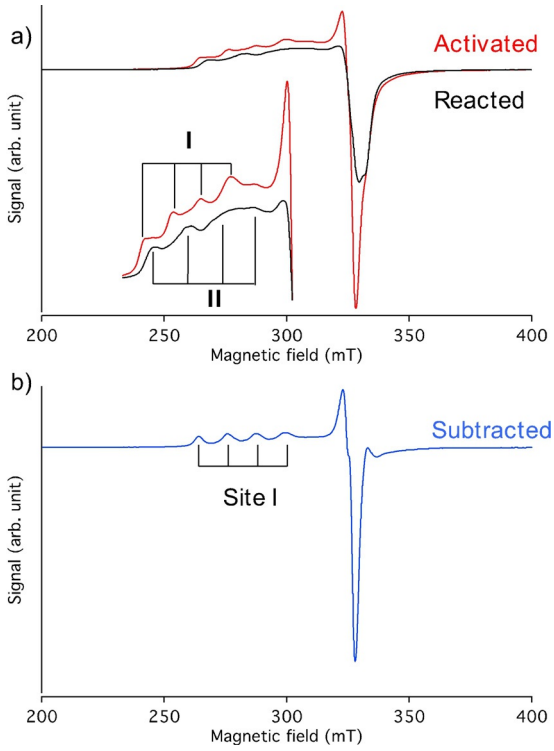

Figure 2. a) In situ X-band EPR spectra (298 K) for **1$_{500}$-γ-a$_{500}$** before and after reaction under 6 bar of CH_4 for 30 min at 200 °C b) X-band EPR difference spectrum (298 K) before–after reaction.

To understand the origin of the observed reactivity, the reaction with CH_4 was monitored by in situ EPR spectroscopy (Figure 2a). For all materials, the initial spectra include a mixture of sites, while after reaction only the signal associated with site I completely disappears, leaving a broad signal consisting of a distribution of unreactive Cu monomers described as site II (Figures 2a, S15,S16). The partial disappearance of the EPR signal can be rationalized by the reduction of reactive Cu^{II} species to EPR-silent Cu^{I}. Furthermore spin quantification, obtained from double integrals of the signal before and after reaction, is consistent with the expected number of electrons ($2e^-$ for CH_4 to CH_3OH) required for the selective reaction with CH_4 (Figure 3a).[24] This Cu^{II}/Cu^{I} redox process is further evidenced by Cu K-edge XANES analysis of material **1$_{500}$-γ-a$_{500}$** before and after reaction, which shows the emergence of a Cu^{I} pre-edge feature (Figure S17) similar to previous reports for zeolitic-[31] and alumina-based systems.[24] Thus, the EPR signal of the reactive Cu^{II} species can be obtained by subtracting the spectra between the reacted and unreacted materials, revealing the spectroscopic signature of the reactive monomeric Cu^{II} site (site I). In contrast to many spectroscopic techniques, which characterize both reactive and spectator Cu^{II} sites, this EPR signature belongs exclusively to the reactive centers involved in the redox reaction.

The maximum ratio of reduced Cu^{II}, determined from the double integrals of the signals before and after reaction, was observed for **1$_{500}$-γ-a$_{500}$** with 32 % of Cu^{I} formed for a CH_3OH

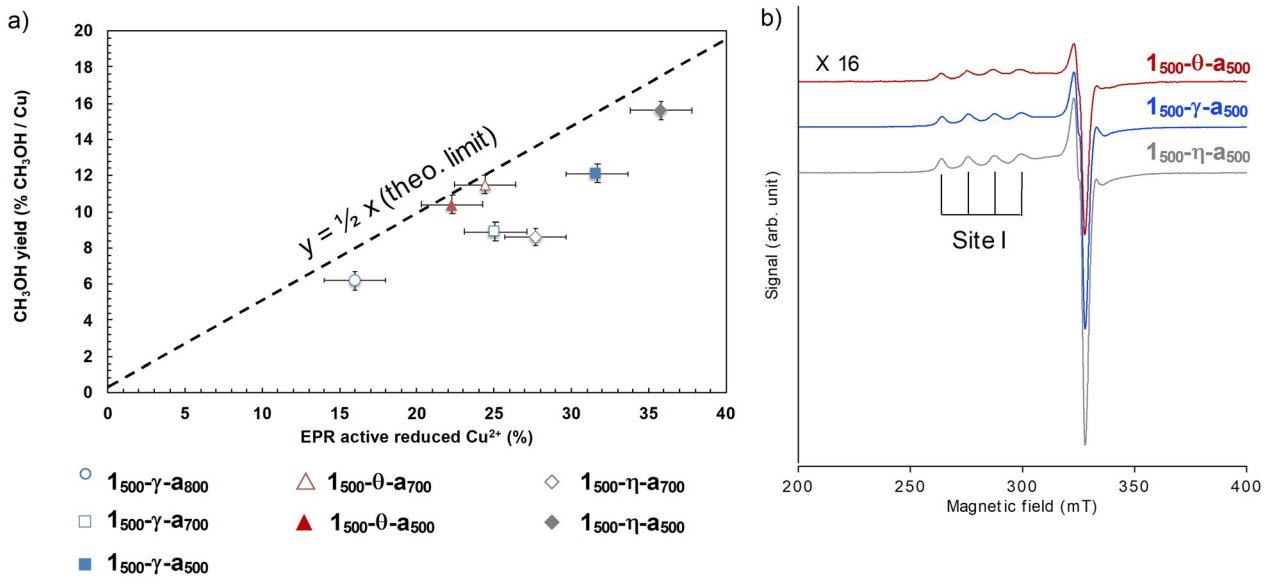

Figure 3. a) Reducibility of the monomeric Cu site determined by double integral of the EPR signal for the initial material less that of the reacted material (in % of Cu) versus CH_3OH yield obtained after reaction with CH_4 in mol CH_3OH mol^{-1} of Cu, for the different Cu supported transition aluminas tested. Deviation from the theoretical limit (dashed line), indicating the two electrons required for the formation of CH_3OH, provides information on the material selectivity toward CH_3OH, and b) X-band difference EPR spectra (298 K) before–after reaction of $\mathbf{1_{500}\text{-}z\text{-}a_{500}}$ supported on various transitional alumina displaying identical reactive Cu^{II} monomeric site I.

yield of 0.12 mol CH_3OH mol^{-1} of Cu (Figure 3 a). Additional information regarding the amount of Cu^{II} centers reduced upon reaction with CH_4 was obtained from linear combination analysis (LCA) of the XANES spectra for $\mathbf{1_{500}\text{-}\gamma\text{-}a_{500}}$; it corresponds to ca. 44 % of Cu^{I} formed upon reaction with methane. The higher proportion of reduced Cu centers obtained from LCA analysis compared to the one obtained by EPR spectroscopy suggests the presence of a small amount of EPR silent reactive Cu^{II} centers, possibly associated with the presence of small antiferromagnetically coupled Cu^{II}-oxo clusters.[32]

To further investigate the presence of small multimeric Cu^{II}-oxo centers, the material was characterized by EXAFS spectroscopy. Cu K-edge EXAFS analysis of $\mathbf{1_{500}\text{-}\gamma\text{-}a_{500}}$ by (Figure S18, Table S2) indicates an average of 3 O in the first coordination sphere of the Cu center and, crucially, the absence of a Cu-Cu path consistent with the presence of mostly Cu^{II} monomers. Comparing the first shell between the initial and reacted states does not reveal significant changes in the local Cu–O coordination sphere (Figure S18, Table S2). Despite the absence of Cu-O-Cu scattering in the deconvolution of the EXAFS, the presence of minor contributions of multimeric Cu^{II} species cannot be excluded.

Further interpretation of the EXAFS is, however, limited by a relatively reduced dataset and low signal-to-noise ratio. Moreover, EXAFS averages over all (both active and inactive) Cu species present; and, in these cases these different contributions cannot be disentangled with any degree of precision or specificity.

By contrast, EPR spectroscopy permits more selective probing of the reactive site (vide supra). Taking advantage of the specificity of this spectroscopy, a wider range of transitional alumina supports was explored (η-, θ- and α-Al_2O_3) to better understand the formation and identity of this reactive monomeric Cu species. Transition aluminas provide different anchoring sites on the support by exposing different low-index planes and facets, although the nature of specific facets remains a matter of debate.

The γ- and η-Al_2O_3 phases are of particular interest because of their high Lewis acidity and similar reactivity.[33] In fact, both are able to coordinate N_2 with a blue shifted IR band at 2355 cm^{-1}, assigned to adsorption at tri-coordinated Al (Al_{III}) for γ-Al_2O_3.[34] Such highly Lewis acidic under-coordinated sites are absent on α-Al_2O_3 surface.

Similar grafting and activation procedures were applied for these different transition aluminas, leading to the generation of well-dispersed Cu^{II} species (Figures S19–S24) supported on Al_2O_3, $\mathbf{1_{500}\text{-}z\text{-}a_X}$ (where "*z*" denotes the phase of the transition alumina employed). Post reaction with CH_4, the surface speciation for each of these materials, was again probed using DRIFTS (Figure S25). Material reactivity was assessed by in situ EPR spectroscopy, coupled with CH_3OH quantification (Figures S26–S30, Table S3).

In all cases, except for $\mathbf{1_{500}\text{-}\alpha\text{-}a_{500}}$, only sites I and II were observed in EPR spectra of the activated material (Figures S26–S29). Upon reaction with CH_4, only site I disappeared.

For $\mathbf{1_{500}\text{-}\alpha\text{-}a_{500}}$, CH_3OH could not be quantified, and the low intensity EPR signal observed for Cu^{II} (Figure S30), likely due to the very low specific surface area (3 $m^2 g^{-1}$) and the small amounts of supported Cu, is unperturbed by reaction with CH_4. The CH_3OH yield measured for all other materials, however, correlates with the disappearance of EPR signal (Figure 3 a) as was previously observed in the case of $\mathbf{1_{500}\text{-}\gamma\text{-}a_X}$. The signal disappearance correspond to the reduction of reactive Cu^{II} sites (sites I), leaving only unreactive Cu^{II} species (sites II).

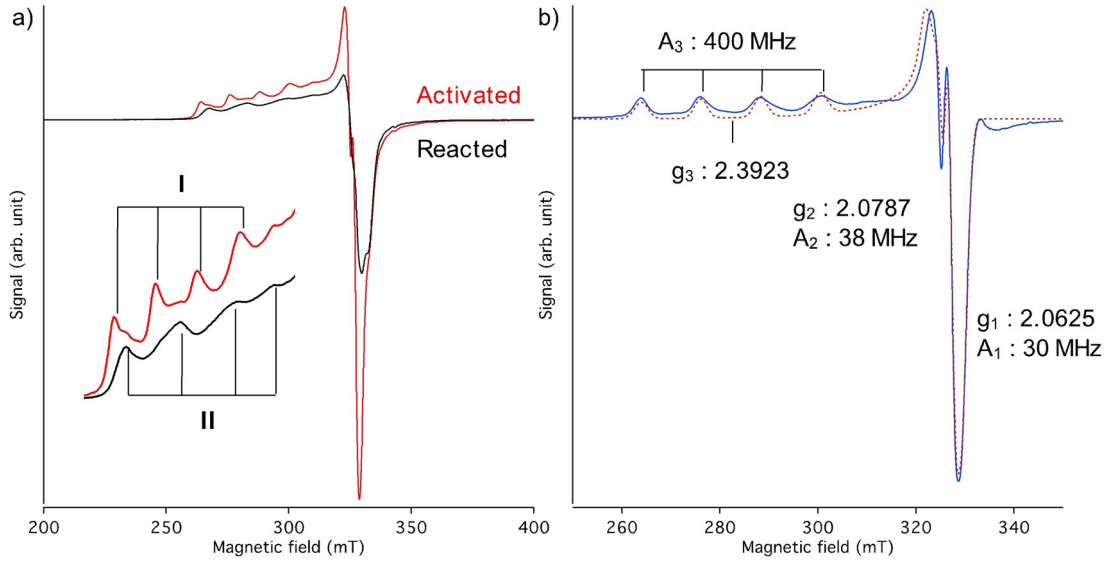

Figure 4. a) X-Band EPR spectra (103 K) for $\mathbf{1}_{500}$-**η**-$\mathbf{a}_{500}$ before and after reaction under 6 bar of CH_4 for 30 min at 200 °C, and b) X-band EPR difference spectrum (103 K) for $\mathbf{1}_{500}$-**η**-$\mathbf{a}_{500}$ before–after reaction (solid line) and the resulting simulation (dashed line) parametrizing the spectrum of the active species.

Greater reactivity is observed for $\mathbf{1}_{500}$-**η**-$\mathbf{a}_{500}$ (0.16 mol $CH_3OH\,mol^{-1}\,Cu$), compared to that for $\mathbf{1}_{500}$-**γ**-$\mathbf{a}_{500}$ (0.12 mol $CH_3OH\,mol^{-1}\,Cu$), which could be rationalize by higher Lewis acidity for **η**-$\mathbf{a}_{500}$ compared to **γ**-$\mathbf{a}_{500}$, and the presence of greater amounts of defective undercoordinated aluminum (Al_{III}) surface sites. These Al_{III}, and their relative amounts, are evidenced by the area of the band of coordinated N_2 observed in the IR spectra of the dehydroxylated Al_2O_3 (Figure S19). This enhanced reactivity suggests that Cu sites are located in close proximity to surface Al_{III} defective sites.[35–37]

Low-temperature CW EPR, and simulation of the EPR parameters, was performed for $\mathbf{1}_{500}$-**η**-$\mathbf{a}_{500}$, which possesses the highest fraction of reactive site I. The EPR spectra of the activated and reacted material for $\mathbf{1}_{500}$-**η**-$\mathbf{a}_{500}$ (Figure 4a) are similar to those observed for $\mathbf{1}_{500}$-**γ**-$\mathbf{a}_{500}$. The resulting difference spectra, corresponding to the reactive, nearly axial, monomeric Cu^{II} species observed on all the materials studied, can be simulated with the g tensor parameters g (site I) = [2.0625 2.0787 2.3923], and hyperfine coupling A_{Cu} (MHz) = [30 38 400] (Figure 4b), while the inactive sites (site II) correspond to at least two distinct species (Supporting Information, Figure S31). Double electron-electron resonance (DEER) measurements of $\mathbf{1}_{500}$-**γ**-$\mathbf{a}_{500}$ before and after reaction with CH_4 (Figure S32) indicates a homogeneous 3D distribution of the Cu^{II} centers, indicating that spatial proximity between the Cu^{II} centers is not necessary for their reactivity.

To gain further insight into the reactive center identity, $\mathbf{1}_{500}$-**γ**-$\mathbf{a}_{500}$ was contacted with CO as a probe molecule and monitored by IR and EPR (Figures S33 & S34). After introduction of 110 mbar of CO, followed by evacuation, new features are observed by IR in the range of 1700–1200 cm^{-1}. The difference between the reacted and activated spectra reveal the appearance of bands at 3611 cm^{-1} (ν_{OH}), 1647 cm^{-1} ($\nu_{s\ OCO}$), 1479 cm^{-1} ($\nu_{s\ OCO}$), 1443 cm^{-1} ($\nu_{s\ OCO}$), 1233 cm^{-1} (δ_{OH}) (Figure 5a & Figure S32). These bands are associated with stable bicarbonate ($HOCO_2^-$) surface intermediates formed during the oxidation of CO, as previously reported for the interaction of CO_2 with γ-Al_2O_3.[38] The same experiment monitored by EPR spectroscopy results in partial disappearance of site I along with appearance of a new EPR signal (Figure 5b & Figure S34).

Difference spectra confirm the involvement of the reactive monomeric Cu^{II} site for the one-electron oxidation of CO to a $HOCO_2^{-\bullet}$ radical anion. Similar reactivity was observed for $\mathbf{1}_{500}$-**η**-$\mathbf{Al_2O_3}_{-500}$ under identical conditions (Figure S35). The new signal, which has an effective g value of 2.0026, possesses an effective super-hyperfine coupling of 50 MHz, as determined from simulation (Figure 5c). The presence of 11 lines for the radical species formed can be explained by hyperfine interaction between the radical center with two equivalent Al nuclei ($A_{eff}(^{27}Al) = 50$ MHz). Similar super-hyperfine couplings were observed by Gafurov et al. upon contacting γ-Al_2O_3 with anthraquinone, which were associated to a tetra-coordinated Al_{IV} pair.[39]

This experiment with CO further supports the assignment of a unique reactive monomeric Cu^{II} species (site I) for the selective conversion of CH_4 to CH_3OH. From the reactivity observed during the one-electron oxidation of carbon monoxide, one can probe the chemical surrounding of the active center. The formation of a bicarbonate radical along with the observed hyperfine coupling constant is consistent with the presence of a hydroxyl group and two equivalent Al_{IV} in the coordination sphere of the reactive Cu^{II} center. We further investigated the reactive species (site I) in $\mathbf{1}_{500}$-**η**-$\mathbf{a}_{500}$, which contains the highest amount of reactive Cu^{II}, with hyperfine sublevel correlation spectroscopy (HYSCORE).[40] Note that the inactive species (site II) in fact did not show characteristic hyperfine couplings in X-band HYSCORE spectra (see Figure S37) such that this method allows for selective observation of the ^1H and ^{27}Al couplings of the reactive species.

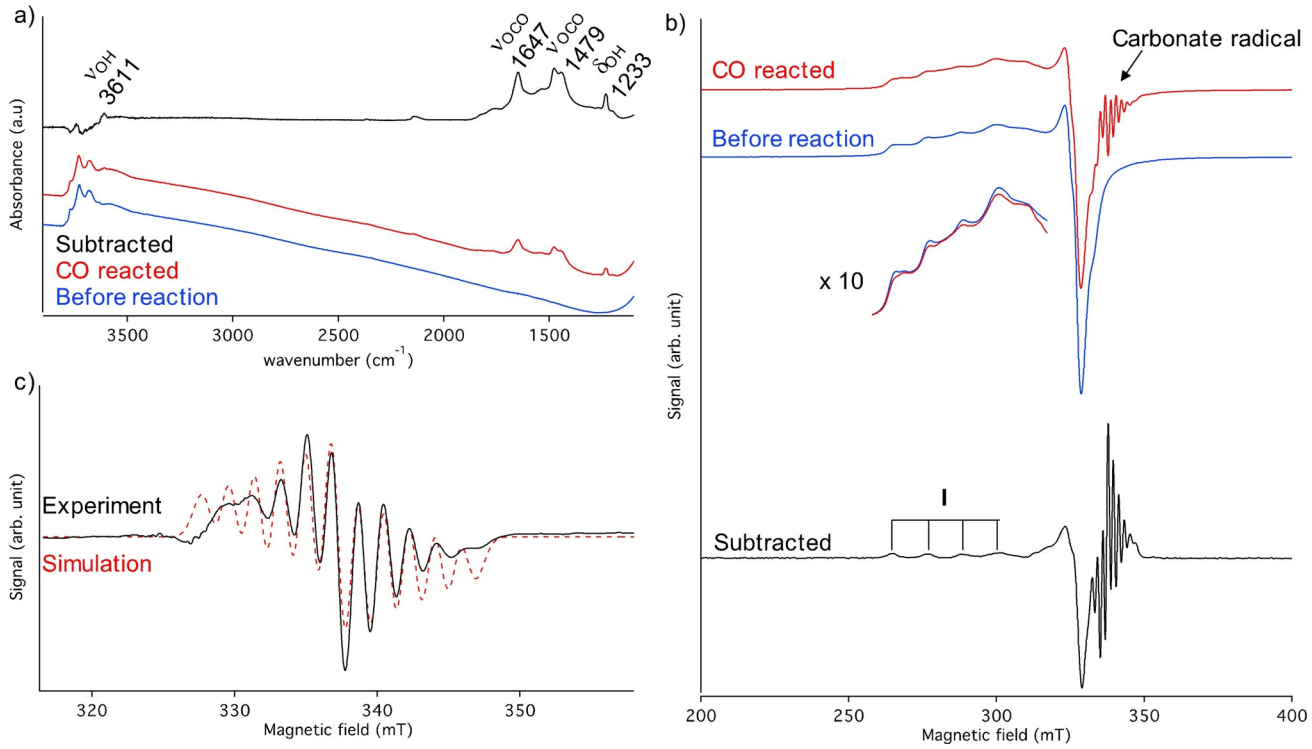

Figure 5. a) FTIR and b) X-band EPR spectra (298 K) of $\mathbf{1}_{500}$-**γ**-$\mathbf{a}_{500}$ before (blue) and after (red) reaction with 110 mbar of CO at room temperature and the corresponding difference spectrum (black). c) Subtracted EPR signal of the carbonate radical formed upon reaction with CO (black) and simulation (dashed red) [g_{eff} = 2.0026 and A_{eff} = 50 MHz].

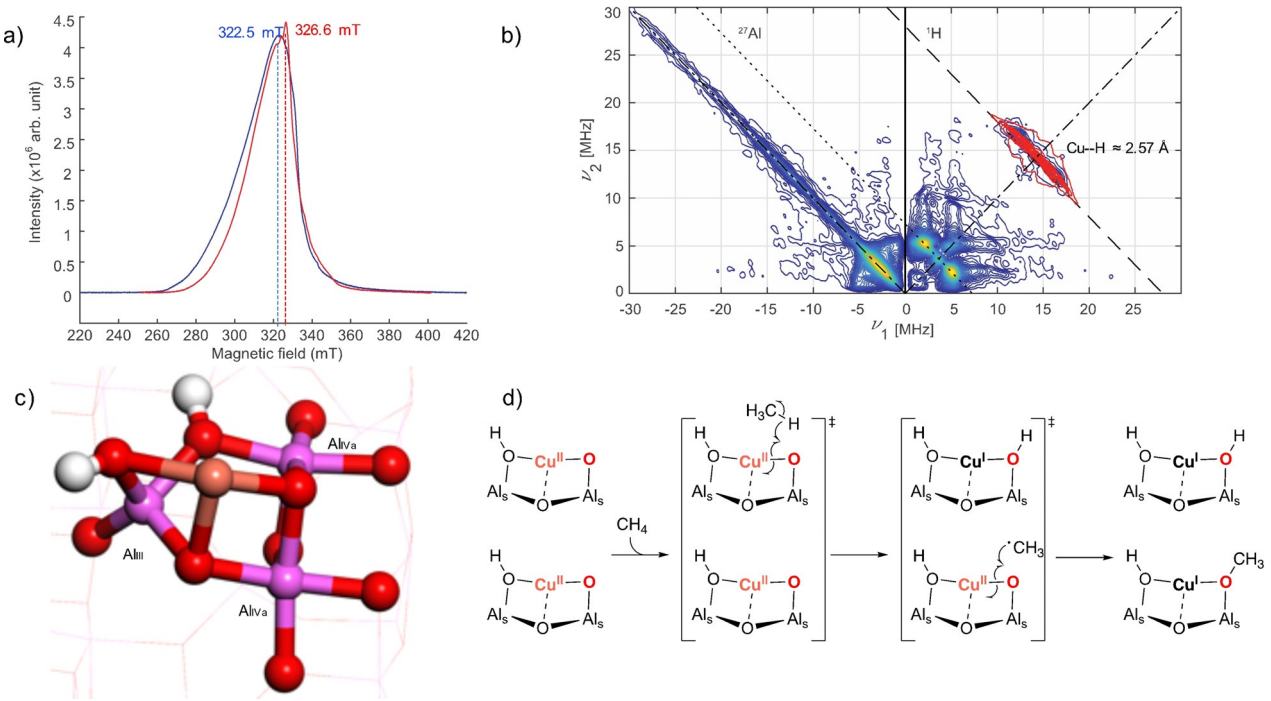

Figure 6. a) X-band echo detected spectra recorded at 10 K for materials before ($\mathbf{1}_{500}$-**η**-$\mathbf{a}_{500}$, red) and after reaction with CH_4 ($\mathbf{1}_{500}$-**η**-$\mathbf{a}_{500}$ **reacted**, blue). The dashed lines indicate the field positions used to record the HYSCORE spectra. b) X-band HYSCORE spectrum of $\mathbf{1}_{500}$-**γ**-$\mathbf{Al_2O_{3-500}}$ at 10 K recorded at the field of 326.6 mT, sum of three spectra with τ = [280 312 400] ns. Spectral intensity along the antidiagonal of (− +) quadrants is caused by phase cycling imperfection. Antidiagonal lines in the HYSCORE spectra indicate nuclear frequencies of ^{1}H (dashed) and ^{27}Al (dotted). The experimental spectrum is displayed in blue to yellow and the simulated ^{1}H ridge in red. c) DFT calculated structure of the reactive tricoordinated $[(Al_2O)CuO(OH)]^-$ site present on the (110) facet of γ-Al_2O_3. d) A possible 2 electron mechanism for CH_4 activation with 2 $[(Al_2O)CuO(OH)]^-$ through hydrogen abstraction followed reaction of the methyl radical.

The HYSCORE spectrum of the reactive species, measured at the magnetic field position corresponding to the maximum intensity of the echo-detected EPR spectrum (Figure 6a), reveals the presence of coupled ^{1}H nuclei in close proximity to the Cu^{II} center, together with a distribution of ^{27}Al couplings (Figure 6b). The HYSCORE spectrum of the reactive species was simulated (Figure 6b & Figure S36), assuming the presence of two equivalent ^{27}Al nuclei, with the related hyperfine and quadrupole couplings of $a_{iso} = 3.39$ MHz, $a_{dip} = [-0.88 \quad 0.03 \quad 0.86]$ MHz, $P = -10.03$ MHz ($\eta = 0.185$). These parameters are quite close to both ^{27}Al hyperfine and quadrupole tensors, estimated for the molecular precursor **1** (see Supporting Information, Section 3). This indicates that the Al atoms of the reactive species possess similar symmetry and coordinative surrounding as in **1**. The ^{1}H hyperfine coupling in $\mathbf{1_{500}\text{-}\eta\text{-}a_{500}}$ was simulated to be $a_{iso} = -0.5 \pm 0.5$ MHz, $a_{dip} = [-4.75 \pm 0.25; \quad -4.75 \pm 0.25; \quad 9.5 \pm 0.5]$ MHz, which corresponds to a Cu-H distance of 2.57 ± 0.05 Å within the point-dipole approximation. Such proton distance is attributed to the presence of hydroxyl group bound to the Cu^{II} active sites.

The presence of a single, unique EPR signature for all reactive Cu^{II} centers (site I) formed on different transition aluminas allows us to refine the geometrical configuration and surrounding environment of this center through combining the experimental evidences derived for the $\mathbf{1_{500}\text{-}\gamma\text{-}Al_2O_{3\text{-}500}}$ and $\mathbf{1_{500}\text{-}\eta\text{-}Al_2O_{3\text{-}500}}$ materials. The Cu^{II} active sites have the following characteristics: i) they possess a coordinated hydroxyl group, ii) they are in close proximity to 2 equivalent Al_{IV} sites, as shown for γ- and η-Al_2O_3 and iii) their formation is correlated to the presence of highly Lewis acidic Al_{III} sites. Such features are strongly reminiscent of the structural characteristics of the (110) facet of γ-Al_2O_3,[41] or the related structures formed at the edge between the (110) and (100) facets.[42] We therefore explored possible structures for the active sites that would feature a characteristic, nearly-axial EPR signature, as well as reasonable formation energies. These Cu^{II} species were modelled by adsorbing a CuO fragment onto various partially hydroxylated configurations of the (110) facet of γ-Al_2O_3 (1 H_2O per unit cell or 3 OH nm^{-2} similar to the experimental OH density for γ-$Al_2O_{3\text{-}500}$ 2.5 OH nm^{-2}—see Supporting Information, Section 8, Figures S38–40). Among these, one model meets all aforementioned experimentally determined requirements (see also Figure S39, model s1a_1). This model corresponds to a tri-coordinated Cu^{II}-oxo site coordinated to two equivalent Al_{IV} and an -OH bound to the so-called Al_{III} with a Cu—H distance of 2.76 Å (Figure 6c). The Cu—H distance is slightly longer than the experimental value (2.76 Å compared to 2.57 Å), likely a result of the shallow potential energy surface. In particular, the T-shape geometry at Cu (Figure 6c) is consistent with the EPR signature of the reactive species featuring a nearly axial g tensor.

Because the partial oxidation of CH_4 to CH_3OH is a two-electron process, two Cu^{II} monomers must be involved since the Cu^{II} sites are reduced to Cu^{I} according to XANES and EPR spectroscopy. This process is feasible via an H-atom abstraction process on the hydroxyl or the oxo bound to Cu^{II}, generating an OH and a methyl radical that will generate a Cu^{I} surface methoxy or CH_3OH species via reaction with a second Cu^{II} site (Figure 6d).

Conclusion

Overall, this study shows that alumina is able to stabilize highly reactive isolated Cu^{II} sites. EPR spectroscopy is shown here to be a particularly powerful characterization method, allowing the exclusive detection of the reactive monomeric sites involved in the partial oxidation of CH_4. The detection of a specific EPR signature for such active sites, $[(Al_2O)CuO\text{-}(OH)]^{-}$, which adopt a T-shape structure, is particularly noteworthy as it opens ways to tailor materials that can stabilize such type of structures. We are currently investigating alternative supports that could stabilize such species with the aim to increase the density of reactive sites.

Acknowledgements

J.M. and M.A.N. thank Shell Global Solutions International B.V. for financial support. We acknowledge Elettra Sincrotrone Trieste for providing access to its synchrotron radiation facilities and we thank Giuliana Aquilanti, Luca Olivi and Danilo Oliveira de Souza for assistance in using XAFS beamline. J.M. acknowledges Dr. Z. Berkson and Dr. D. Mance for their help conducting and analyzing the NMR experiments.

Conflict of interest

The authors declare no conflict of interest.

Keywords: alumina · copper · EPR spectroscopy · methane-to-methanol · surface organometallic chemistry

[1] J. P. Lange, K. P. De Jong, J. Ansorge, P. J. A. Tijm, *Stud. Surf. Sci. Catal.* **1997**, *107*, 81–86.
[2] M. Ahlquist, R. J. Nielsen, R. A. Periana, W. A. Goddard, *J. Am. Chem. Soc.* **2009**, *131*, 17110–17115.
[3] M. Ravi, M. Ranocchiari, J. A. van Bokhoven, *Angew. Chem. Int. Ed.* **2017**, *56*, 16464–16483; *Angew. Chem.* **2017**, *129*, 16684–16704.
[4] A. A. Latimer, A. Kakekhani, A. R. Kulkarni, J. K. Nørskov, *ACS Catal.* **2018**, *8*, 6894–6907.
[5] T. J. Lawton, A. C. Rosenzweig, *J. Am. Chem. Soc.* **2016**, *138*, 9327–9340.
[6] S. I. Chan, V. C. C. Wang, J. C. H. Lai, S. S. F. Yu, P. P. Y. Chen, K. H. C. Chen, C. L. Chen, M. K. Chan, *Angew. Chem. Int. Ed.* **2007**, *46*, 1992–1994; *Angew. Chem.* **2007**, *119*, 2038–2040.
[7] R. Balasubramanian, S. M. Smith, S. Rawat, L. A. Yatsunyk, T. L. Stemmler, A. C. Rosenzweig, *Nature* **2010**, *465*, 115–119.
[8] M. O. Ross, F. MacMillan, J. Wang, A. Nisthal, T. J. Lawton, B. D. Olafson, S. L. Mayo, A. C. Rosenzweig, B. M. Hoffman, *Science* **2019**, *364*, 566–570.
[9] R. L. Lieberman, A. C. Rosenzweig, *Nature* **2005**, *434*, 177–182.
[10] E. V. Starokon, M. V. Parfenov, L. V. Pirutko, S. I. Abornev, G. I. Panov, *J. Phys. Chem. C* **2011**, *115*, 2155–2161.

[11] M. H. Groothaert, P. J. Smeets, B. F. Sels, P. A. Jacobs, R. A. Schoonheydt, *J. Am. Chem. Soc.* **2005**, *127*, 1394 – 1395.
[12] M. A. Newton, A. J. Knorpp, V. L. Sushkevich, D. Palagin, J. A. Van Bokhoven, *Chem. Soc. Rev.* **2020**, *49*, 1449 – 1486.
[13] J. S. Woertink, P. J. Smeets, M. H. Groothaert, M. A. Vance, B. F. Sels, R. A. Schoonheydt, E. I. Solomon, *Proc. Natl. Acad. Sci. USA* **2009**, *106*, 18908 – 18913.
[14] S. Grundner, M. A. C. Markovits, G. Li, M. Tromp, E. A. Pidko, E. J. M. Hensen, A. Jentys, M. Sanchez-Sanchez, J. A. Lercher, *Nat. Commun.* **2015**, *6*, 7546.
[15] A. R. Kulkarni, Z. J. Zhao, S. Siahrostami, J. K. Nørskov, F. Studt, *ACS Catal.* **2016**, *6*, 6531 – 6536.
[16] V. L. Sushkevich, D. Palagin, J. A. van Bokhoven, *Angew. Chem. Int. Ed.* **2018**, *57*, 8906 – 8910; *Angew. Chem.* **2018**, *130*, 9044 – 9048.
[17] A. Knorpp, A. B. Pinar, C. Baerlocher, L. B. McCusker, N. Casati, M. A. Newton, S. Checchia, J. Meyet, D. Palagin, J. A. van Bokhoven, *Angew. Chem. Int. Ed.* **2021**, *60*, 5854 – 5858; *Angew. Chem.* **2021**, *133*, 5918 – 5922.
[18] D. K. Pappas, A. Martini, M. Dyballa, K. Kvande, S. Teketel, K. A. Lomachenko, R. Baran, P. Glatzel, B. Arstad, G. Berlier, et al., *J. Am. Chem. Soc.* **2018**, *140*, 15270 – 15278.
[19] J. P. Lange, V. L. Sushkevich, A. J. Knorpp, J. A. Van Bokhoven, *Ind. Eng. Chem. Res.* **2019**, *58*, 8674 – 8680.
[20] Z. R. Jovanovic, J. P. Lange, M. Ravi, A. J. Knorpp, V. L. Sushkevich, M. A. Newton, D. Palagin, J. A. van Bokhoven, *J. Catal.* **2020**, *385*, 238 – 245.
[21] H. V. Le, S. Parishan, A. Sagaltchik, H. Ahi, A. Trunschke, R. Schomäcker, A. Thomas, *Chem. Eur. J.* **2018**, *24*, 12592 – 12599.
[22] S. E. Bozbag, P. Sot, M. Nachtegaal, M. Ranocchiari, J. A. Van Bokhoven, C. Mesters, *ACS Catal.* **2018**, *8*, 5721 – 5731.
[23] X. Wang, N. M. Martin, J. Nilsson, S. Carlson, J. Gustafson, M. Skoglundh, P. A. Carlsson, *Catalysts* **2018**, *8*, 545.
[24] J. Meyet, K. Searles, M. A. Newton, M. Wörle, A. P. van Bavel, A. D. Horton, J. A. van Bokhoven, C. Copéret, *Angew. Chem. Int. Ed.* **2019**, *58*, 9841 – 9845; *Angew. Chem.* **2019**, *131*, 9946 – 9950.
[25] C. Copéret, *Nat. Energy* **2019**, *4*, 1018 – 1024.
[26] M. Veith, K. Valtchev, V. Huch, *Inorg. Chem.* **2008**, *47*, 1204 – 1217.
[27] H. J. Jang, W. K. Hall, J. L. D'Itri, *J. Phys. Chem.* **1996**, *100*, 9416 – 9420.
[28] V. L. Sushkevich, J. A. Van Bokhoven, *Chem. Commun.* **2018**, *54*, 7447 – 7450.
[29] T. P. Beebe, J. E. Crowell, J. T. Yates, *J. Chem. Phys.* **1990**, *92*, 5119 – 5126.
[30] A. Comas-Vives, M. Schwarzwälder, C. Copéret, P. Sautet, *J. Phys. Chem. C* **2015**, *119*, 7156 – 7163.
[31] M. A. Newton, A. J. Knorpp, A. B. Pinar, V. L. Sushkevich, D. Palagin, J. A. Van Bokhoven, *J. Am. Chem. Soc.* **2018**, *140*, 10090 – 10093.
[32] A. Godiksen, F. N. Stappen, P. N. R. Vennestrøm, F. Giordanino, S. B. Rasmussen, L. F. Lundegaard, S. Mossin, *J. Phys. Chem. C* **2014**, *118*, 23126 – 23138.
[33] G. Busca, *Adv. Catal.* **2014**, *57*, 319 – 404.
[34] D. S. Maciver, H. H. Tobin, R. T. Barth, *J. Catal.* **1963**, *2*, 485 – 497.
[35] S. A. Zubkov, V. Y. Borovkov, S. G. Gagarin, V. B. Kazansky, *Chem. Phys. Lett.* **1984**, *107*, 337 – 340.
[36] R. Wischert, C. Copéret, F. Delbecq, P. Sautet, *Chem. Commun.* **2011**, *47*, 4890 – 4892.
[37] R. Wischert, P. Laurent, C. Copéret, F. Delbecq, P. Sautet, *J. Am. Chem. Soc.* **2012**, *134*, 14430 – 14449.
[38] J. Szanyi, J. H. Kwak, *Phys. Chem. Chem. Phys.* **2014**, *16*, 15117 – 15125.
[39] M. R. Gafurov, I. N. Mukhambetov, B. V. Yavkin, G. V. Mamin, A. A. Lamberov, S. B. Orlinskii, *J. Phys. Chem. C* **2015**, *119*, 27410 – 27415.
[40] P. Höfer, A. Grupp, H. Nebenführ, M. Mehring, *Chem. Phys. Lett.* **1986**, *132*, 279 – 282.
[41] M. Digne, P. Sautet, P. Raybaud, P. Euzen, H. Toulhoat, *J. Catal.* **2002**, *211*, 1 – 5.
[42] A. T. F. Batista, D. Wisser, T. Pigeon, D. Gajan, F. Diehl, M. Rivallan, L. Catita, A.-S. Gay, A. Lesage, C. Chizallet, et al., *J. Catal.* **2019**, *378*, 140 – 143.

Manuscript received: April 19, 2021
Version of record online: June 15, 2021

